Fracture Mechanics of Concrete and Concrete Structures -
Recent Advances in Fracture Mechanics of Concrete - B. H. Oh, et al.(eds)

Investigation on time-dependent fracture mechanism of mortar based on meso-scale numerical approach

K. Matsumoto
Tokyo Institute of Technology, Tokyo, Japan

Y. Sato
Hokkaido University, Sapporo, Japan

T. Ueda
Hokkaido University, Sapporo, Japan

ABSTRACT: To investigate time-dependent fracture mechanism of mortar, discrete numerical analysis by Rigid Body Spring Model (RBSM) was conducted. Four-Components Combined Model and Pseudo Monotonic Loading developed by authors were used for constitutive law and for determining failure state, respectively. The analysis could express reasonable results in terms of strength, stiffness and global stress-strain relationship observed in macro level. This study focuses on behavior in meso level as well. Through an investigation on stress-strain-time response of connected springs, fracture process of mortar under creep loading was examined. As a result, fracture mechanism, in which stress redistribution caused due to stress relaxation in uncracked portion leads new cracks to be formed, was determined.

1 INTRODUCTION

Mechanical deterioration due to time-dependent loads such as fatigue and creep is one of the most primary issues in maintenance for infrastructures. In current design, fatigue is represented by S-N curve and cumulative damage law. Using these methods, structural design engineers can examine period to have a failure (*Safety Verification*.) However, the other structural performances such as serviceability and durability cannot be examined because deformation and cracking during the service life is unknown. Besides, demand of rehabilitation cannot be discussed because residual strength is also unknown.

Past studies of fatigue subjected to properties other than fatigue life generally have been experimental studies of stress-strain characteristics (For example, Hatano et al. 1979, Muguruma et al. 1970) These studies clarified the relationship between concrete deformation and fatigue loading cycle, the transition of unloading-reloading curve, and changes in the internal stiffness. Analytical studies are now starting to be applied. Tanabe et al. (1998) analytically expressed the effect of the strain rate and unloading/reloading on concrete behavior using a rheological model. El-Kashif et al. (2004) proposed a time-dependent concrete constitutive model that incorporates a time effect into the stress-strain relationship. Maekawa et al. (2006) carried out fatigue FE analysis of concrete members by extending El-Kashif's model to the fatigue problem.

When concrete is subjected to long-term mechanical actions, environmental condition strongly affects its behavior. On the other hand, continuous modeling as mentioned above is difficult to be applied to the actual environmental actions because it does not take into account material information in micro level. Meso-scale modeling, in which concrete is treated as heterogeneous material and the material information in micro level is directly introduced, can be a solution.

In this study, meso-scale numerical analysis of mortar, which is a main constituent of concrete, was conducted subjected to monotonic and creep loading. Obtained results were compared with the experiment in terms of fatigue life, global stress-global strain characteristics, and crack patterns. In addition, fracture process was verified using meso-scale approach in this study. That is, fracture mechanism of mortar was investigated with discussing in terms of stress relaxation, redistribution and micro crack development.

2 METHOD OF THE ANALYSIS

The RBSM (Rigid Body Spring Model) developed by Kawai and Takeuchi employs a discrete numerical analysis method (Kawai 1977). Compared with common discrete analysis methods, such as the Distinct Element Method (Cundall & Strack 1979), RBSM is suitable for small deformation problems. Bolander & Saito (1998), Ueda et al. (1988) and Nagai et al. (2004) have used RBSM for analysis of cement-based materials and structures.

In RBSM, the analytical model is divided into polyhedron elements whose faces are interconnected by springs as shown in Figure 1. Each element has two transitional and one rotational degree of freedom at the center of gravity. Normal and shear springs are placed at the boundary of the elements. Since cracks initiate and propagate along the boundary face, the mesh arrangement may affect fracture direction. To avoid the formation of cracks in a certain direction, random geometry is introduced using a Voronoi diagram. A Voronoi diagram is a collection of Voronoi cells. Each cell represents a mortar element in the analysis. For Voronoi meshing, geometric computational software developed by Sugihara (1998) is applied. Size of each element is controlled to be 2-3 [mm^2].

In the nonlinear analysis, a stiffness matrix is constructed on the principle of virtual work (Kawai & Takeuchi 1990), and the Modified Newton-Raphson method is employed for the convergence algorithm. In the convergence process, displacements that cancel the unbalanced force of elements are added to the elements. The displacements are calculated using the stiffness matrix. Convergence in the model occurs when the ratio of the sum of the squares of the unbalanced forces of the elements in the model to the sum of the squares of applied force becomes less than 10^{-5}. When the model does not converge at the given maximum iterative calculation number, analysis proceeds to the next step. The maximum iterative number is set to 100 in this study. These values were determined based on sensitivity analysis. The remaining unbalanced forces of elements after the iteration process are added at the next step.

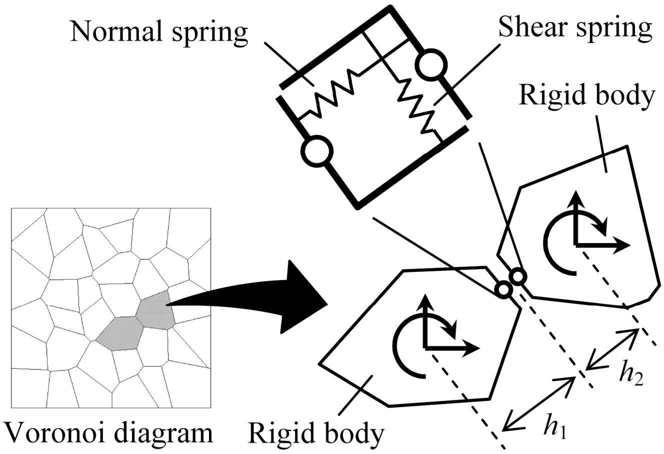

Figure 1. Concept of RBSM.

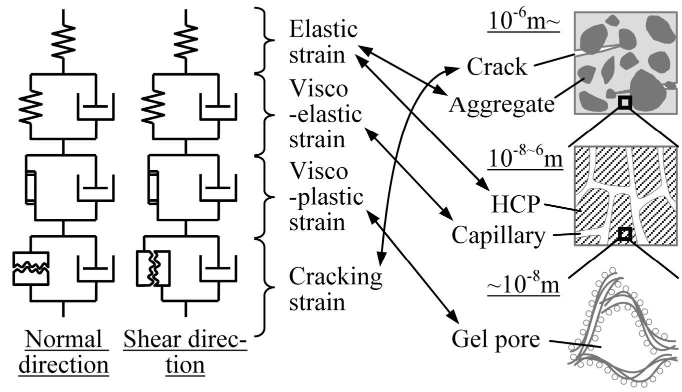

Figure 2. Four Components Combined Model.

Visco-elastic component is reversible but time-dependent deformation in uncracked portion. This component is related to water movement in capillary pores. Since capillary pores have comparatively large structure ($10^{-8\sim-6}$m), rate of this deformation is relatively high and reversible.

Visco-plastic component is irreversible and time-dependent deformation in uncracked portion. This component is related to water movement in gel pores. Since gel pores have comparatively small structure (10^{-9}~10^{-8} m), rate of this deformation is relatively slow and irreversible.

Cracking component is crack opening displacement (COD) and crack sliding displacement (CSD) in normal and shear direction, respectively. Stress transfer mechanisms in normal and shear direction are bridging and interlock effect of aggregates between crack surfaces. Therefore, this component has time-dependency because their mechanical behavior is governed by interface between aggregate and cement paste.

3 CONSTITUTIVE MODEL

3.1 *Basic concept*

Figure 2 shows mechanical model used in this study. Total deformation is expressed by a summation of deformation of cracked and uncracked portion both in normal and shear direction. Additionally, deformation of uncracked portion is separated into elastic, visco-elastic and visco-plastic component. Phenomenal descriptions of each component are as follows.

Elastic component is reversible and instantaneous (time-independent) deformation in uncracked portion. This component corresponds to elastic deformation of fine aggregate and hardened cement paste contained in mortar.

3.2 *Elastic component*

Elastic component is composed of an elastic spring. The stress-strain relationship follows Hooke's law.

$$\begin{aligned} \sigma_e &= k_e \varepsilon_e \\ \tau_e &= G_e \gamma_e \end{aligned} \tag{1}$$

where, σ_e is stress of elastic component spring (normal direction), k_e is spring constant of elastic component (normal direction), ε_e is elastic strain (normal direction), τ_e is stress of elastic component spring (shear direction), G_e is spring constant of elastic component (shear direction), γ_e is elastic strain (shear direction).

3.3 *Visco-plastic component*

Visco-elastic component is composed of elastic spring and dashpot. Stress-strain relationship of the elastic spring follows Hooke's law.

$$\begin{aligned}\sigma_{ve} &= k_{ve}\varepsilon_{ve} \\ \tau_{ve} &= G_{ve}\gamma_{ve}\end{aligned} \tag{2}$$

where, σ_{ve} is stress of visco-elastic spring (normal direction), k_{ve} is spring constant of visco-elastic component (normal direction), ε_{ve} is visco-elastic strain (normal direction), τ_{ve} is stress of visco-elastic spring (shear direction), G_{ve} is spring constant of visco-elastic component (shear direction), γ_{ve} is visco-elastic strain (shear direction).

Stress-strain rate relationship of the dashpot follows Newtonian viscosity law.

$$\begin{aligned}\sigma_{ved} &= \mu_{ven}\frac{d\varepsilon_{ve}}{dt} \\ \tau_{ved} &= \mu_{ves}\frac{d\gamma_{ve}}{dt}\end{aligned} \tag{3}$$

where, σ_{ved} is stress of visco-elastic dashpot (normal direction), μ_{ven} is viscosity coefficient for visco-elastic component (normal direction), $d\varepsilon_{ve}/dt$ is strain rate of visco-elastic component (normal direction), τ_{ved} is stress of visco-elastic dashpot (shear direction), μ_{ves} is viscosity coefficient for visco-elastic component (shear direction), $d\gamma_{ve}/dt$ is strain rate of visco-elastic component (shear direction).

3.4 *Visco-plastic component*

Visco-plastic component is composed of plastic slider and dashpot. Figure 3 shows stress-strain relationship of the plastic slider in normal and shear direction. Where, ε_{vp} is positive in tension.

Stress-strain rate relationship of the dashpot was determined by exponential function as following.

$$\begin{aligned}\sigma_{vpd} &= \frac{\mu_{vpn}}{A^{B-1}B}\left[\left(\frac{d\varepsilon_{vp}}{dt}+A\right)^B - A^B\right] \\ \tau_{vpd} &= \frac{\mu_{vps}}{A^{B-1}B}\left[\left(\frac{d\gamma_{vp}}{dt}+A\right)^B - A^B\right]\end{aligned} \tag{4}$$

where, σ_{vpd} is stress of visco-plastic dashpot (normal direction), μ_{vpn} is viscosity coefficient for visco-plastic component (normal direction), $d\varepsilon_{vp}/dt$ is strain rate of visco-plastic component (normal direction), τ_{vpd} is stress of visco-plastic dashpot (shear direction), μ_{vps} is viscosity coefficient for visco-plastic component (shear direction), $d\gamma_{vp}/dt$ is strain rate of visco-plastic component (shear direction), A and B are coefficients for representing nonlinearity (A=10^{-10}, B=10^{-3}).

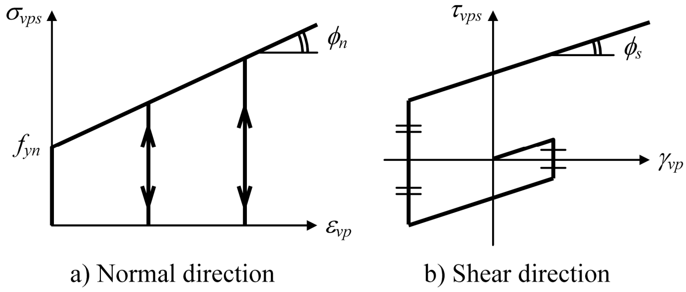

Figure 3. Stress-strain model for slider elements.

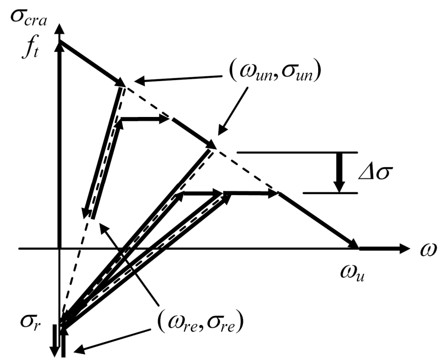

Figure 4. Model for tension softening element.

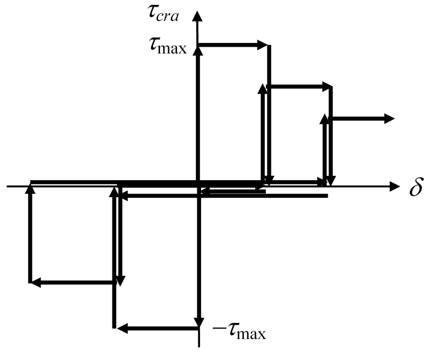

Figure 5. Model for shear transferring element.

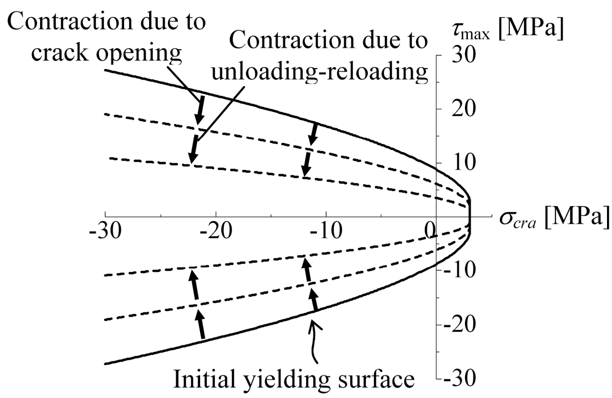

Figure 6. Yielding criteria for shear transferring element.

3.5 *Cracking component*

For normal direction, cracking component is composed of tension softening element and dashpot. For shear direction, cracking component is composed of shear transfer element and dashpot. Tension softening and shear transfer at crack surface are described by crack opening displacement (COD) and crack sliding displacement (CSD), respectively. Relationship between strain and displacement is given as following.

$$\begin{aligned} \omega &= (h_1 + h_2)\varepsilon_{cra} \\ \delta &= (h_1 + h_2)\gamma_{cra} \end{aligned} \tag{5}$$

where, ω is crack opening displacement (COD), h_1 and h_2 are length of perpendicular lines from element gravity point to the boundary face as shown in Figure 1, ε_{cra} is crack induced average strain (normal direction), δ is crack sliding displacement (CSD), γ_{cra} is crack induced average strain (shear direction).

Figure 4 shows stress-displacement relationship of tension softening element. $\Delta\sigma$ in the figure represents stress decrease during unloading-reloading in the softening branch and given as following.

$$\Delta\sigma = c_{yn}\sigma_{un}{}^{\alpha}(\sigma_{un} - \sigma_{re}) \tag{6}$$

where, c_{yn} is constant, σ_{un} is stress of plastic slider when it is started to be unloaded, α is coefficient for representing nonlinearity, σ_{re} is stress of plastic slider when it is started to be reloaded.

Figure 5 shows stress-displacement relationship of shear transfer element. In this study, rigid-plastic model is employed. However, yielding strength $\tau_{\max}$ changes associated with stress of tension softening element as shown in Figure 6. Where, initial yielding surface is given as following.

$$\tau_{\max i} = \pm\left[0.11 f_t^3(-\sigma_{cra} + f_t)^{0.6} + f_t\right] \tag{7}$$

To take into account the effect of unloading-reloading and crack opening on shear transfer behavior, coefficients f_1 and f_2 for representing surface contraction were introduced by following equations.

$$\begin{aligned} f_1 &= 1 - \frac{\omega}{\omega_u} \\ f_2 &= 1 - c_{ys}\tau_{un}{}^{\beta}(\tau_{un} - \tau_{re}) \\ &(f_1, f_2 \geq 0) \end{aligned} \tag{8}$$

where, f_1 is coefficient for surface contraction due to crack opening, f_2 is coefficient for surface contraction due to unloading-reloading, c_{ys} is constant, τ_{un} is shear stress when it is started to be unloaded, β is coefficient for representing nonlinearity, τ_{re} is shear stress when it is started to be reloaded.

Yielding strength $\tau_{\max}$ is given as following.

$$\tau_{\max} = f_1 \times f_2 \times \tau_{\max i} \tag{9}$$

Stress-strain rate relationship of the dashpot is given by logarithm function as following.

$$\begin{aligned} \sigma_{crad} &= \mu_{cran} \ln\left[\frac{d\varepsilon_{cra}}{dt} + 1\right] \\ \tau_{crad} &= \mu_{cras} \ln\left[\frac{d\gamma_{cra}}{dt} + 1\right] \end{aligned} \tag{10}$$

where, σ_{crad} is stress of dashpot of cracking component (normal direction), μ_{cran} is viscosity coefficient for cracking component (normal direction), $d\varepsilon_{cra}/dt$ is strain rate of cracking component (normal direction), τ_{crad} is stress of dashpot of cracking component (shear direction), μ_{cras} is viscosity coefficient for cracking component (shear direction), $d\gamma_{cra}/dt$ is strain rate of cracking component (shear direction).

Stress transfer at crack surface is caused by aggregate bridging and interlock effect. That is, viscosity of the cracking component is derived from time effect in deformation of aggregate, cement matrix and their interface. Therefore, if the bridging and interlock effect are lost associated with crack opening, viscosity of cracking component is also lost. Consequently, reduction function for viscosity coefficient of cracking component was introduced as follows.

$$\begin{aligned} \mu_{cran} &= \mu_{cran0}\left(1 - \frac{\omega}{\omega_u}\right) \\ \mu_{cras} &= \mu_{cras0}\left(1 - \frac{\omega}{\omega_u}\right) \end{aligned} \tag{11}$$

where, μ_{cran0} is initial value of viscosity coefficient for cracking component (normal direction), μ_{cras0} is initial value of viscosity coefficient for cracking component (shear direction).

3.6 *Relationship among each component*

Among the stress and strain of each component, following equations are satisfied because of force and deformational equilibrium.

$$\begin{aligned} \varepsilon &= \varepsilon_e + \varepsilon_{ve} + \varepsilon_{vp} + \varepsilon_{cra} \\ \gamma &= \gamma_e + \gamma_{ve} + \gamma_{vp} + \gamma_{cra} \\ \sigma &= \sigma_e = \sigma_{ve} + \sigma_{ved} = \sigma_{vp} + \sigma_{vpd} = \sigma_{cra} + \sigma_{crad} \\ \tau &= \tau_e = \tau_{ve} + \tau_{ved} = \tau_{vp} + \tau_{vpd} = \tau_{cra} + \tau_{crad} \end{aligned} \tag{12}$$

where, ε is total strain, σ is total stress.

3.7 *Model constants*

The authors developed a scheme for determining constants used in the constitutive model in the previous study (Matsumoto et al. 2008). All constants are determined from production condition of mortar, which is mix proportion (water W, cement C, and sand S) and curing period (t). First, mechanical properties of mortar (compressive strength, tensile strength, elastic modulus, and creep coefficient) are calculated from the production condition. Second, mechanical properties in meso level taking into account heterogeneity of the material are calculated using probability density function. Last, model constants are determined using functions, which were based on the result of parametric analyses. Figure 7 shows flow to determine model constants. For detail, see the author's previous study (Matsumoto et al. 2008).

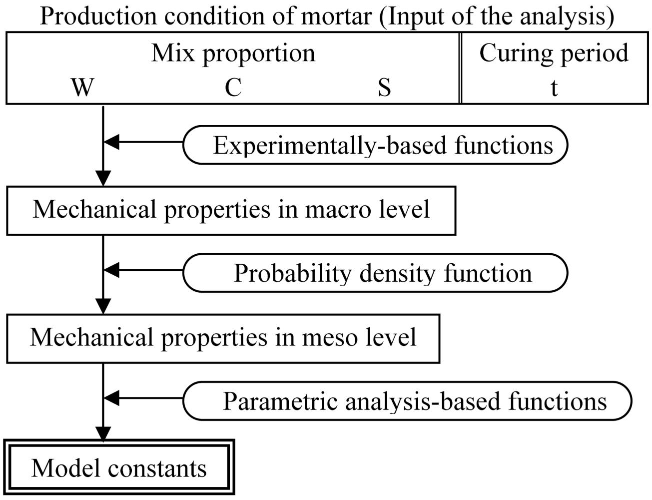

Figure 7. Flow for determining model constants.

4 SIMULATION OF MORTAR FAILURE

4.1 *Outline*

Figure 8 shows mortar model used in the analyses. Size of the specimen is 75 mm x 150 mm containing 3,200 Voronoi cells. In this study, shape of the element is different for each analytical case because meshing process is reapplied. Load is applied on top surface of the specimen under load or displacement control.

Table 1 lists analytical cases conducted in this study. They include 2 types of loading that are monotonic and creep loading. In this study, computation was carried out 3 times for each analytical case with changing shape of the element and variation of the material properties in meso level given by probability density function mentioned in 3.7 to examine variation of the analytical result.

The analyses subjected to creep loading are conducted under load controlled condition. Since load is forcibly given in load controlled analysis, failure state cannot be evaluated from load-displacement response. Therefore, this study employed a method for determining failure developed by the authors (Matsumoto et al. 2008). Figure 9 shows the basic concept. This method is based on the definition that failure occurs when the material strength becomes less than the applied stress. That is, displacement controlled analysis called pseudo monotonic loading is conducted at a certain time interval. If residual strength obtained in the pseudo monotonic loading becomes smaller than the applied stress, the analysis makes failure determination.

4.2 *Analyses under monotonic loading*

Case MC40000, MC4000, MC400, MC40A, MC40B, MTA and MTB are subjected to monotonic loading. Former 5 cases are in compression and latter 2 cases are in tension. For MC40000, MC4000, MC400 and MC40A, production condition is same but the applied strain rate is varied from 40 to 40000 mic/sec. Applied strain rate in MC40B is also 40 mic/sec as well as MC40A, but the input of mix proportion is different. For MTA and MTB, applied strain rate is same (4 mic/sec) but the input of mix proportion is different. Load is applied under displacement controlled condition for all cases.

In this study, global strain and global stress are defined as displacement at the top surface divided by specimen height and applied force at the top surface

Table 1. List of analytical cases conducted in this study.

Case	Loading condition Type	Direction	Others	Production condition W [kg/m^3]	C [kg/m^3]	S [kg/m^3]	t [days]
MC40000	Monotonic	Comp.	Strain rate=40000 mic/sec	310	620	1240	28
MC4000			Strain rate=4000 mic/sec				
MC400			Strain rate=400 mic/sec				
MC40A			Strain rate=40 mic/sec				
MC40B				209	523	1569	
MTA		Ten.	Strain rate=4 mic/sec	310	620	1240	
MTB							
CC80	Creep	Comp.	Creep stress ratio=0.8	209	523	1569	
CC14.8MPa			Creep stress =14.8 MPa				
CC10.2MPa			Creep stress =10.2 MPa				
CT		Ten.	Creep stress ratio=0.9				

divided by sectional area, respectively. Figure 10 and 11 show global stress-global strain relationships obtained in MC40A, MC40B, MTA and MTB. Mix proportions of mortar affect the mechanical behavior, that is, strength and stiffness become higher with smaller water-cement ratio as observed in the experiment. Figure 12 shows compressive strength-applied strain rate relationship obtained in MC40000, MC4000, MC400 and MC40A. Where, the strength is normalized by that in MC40A. The figure includes experimental result by Li et al. (1998), Jingyao et al. (2002) and Shraddhakar et al. (1990). The analysis could simulate strength enhancement of mortar under higher strain rates. Variation of the strength obtained in the analyses is slightly smaller than that in the experiment. This is because experimental results contain not only strength variation but also effect of mix proportion, loading accuracy and environmental condition.

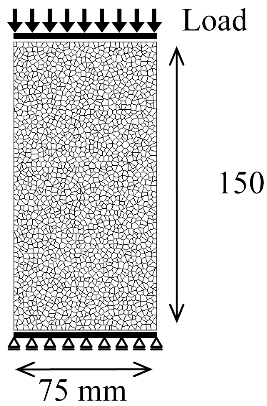

Figure 8. Mortar model (meshing pattern is dif-ferent for each analytical case).

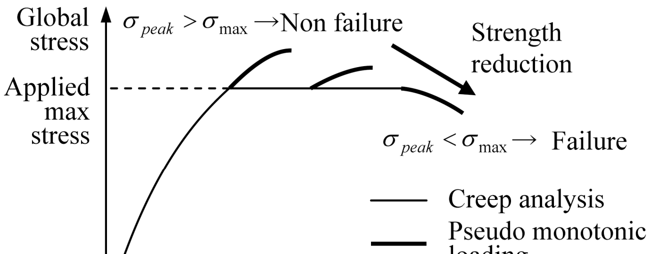

Figure 9. Method for determining failure.

4.3 *Analyses under creep loading*

Case CC80, CC14.8MPa, CC10.2MPa and CT are subjected to creep loading. Former 3 cases are in compression and latter 1 case is in tension. For this series, load is applied under load controlled condition. Applied load level is varied among CC80, CC14.8MPa and CC10.2MPa. For CC80, the load level is controlled so that the global stress agrees with 80% of average strength in MC40B. That is, creep stress-strength ratio in this case is 0.8. For CC14.8MPa and CC10.2MPa, the load is not controlled by stress-strength ratio but by stress itself. Applied global stress for CC14.8MPa and CC10.2MPa is 14.8 and 10.2 MPa, respectively. These stresses and the input of mix proportion are same as those used in the creep loading test by Neville (1959). These cases have unloading process to verify creep recovery behavior. For CT, the load level is controlled so that the global stress agrees with 90% of average strength in MTB (creep stress-strength ratio=0.9).

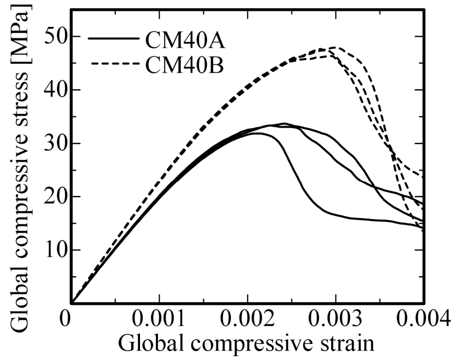

Figure 10. Global stress-strain under monotonic comp. loading.

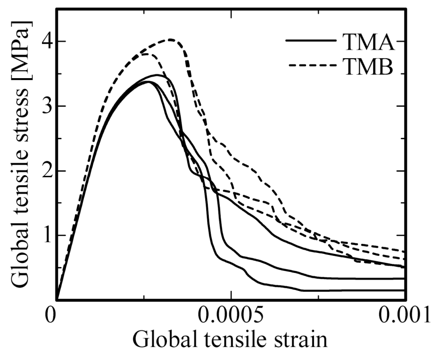

Figure 11. Global stress-strain under monotonic tensile loading.

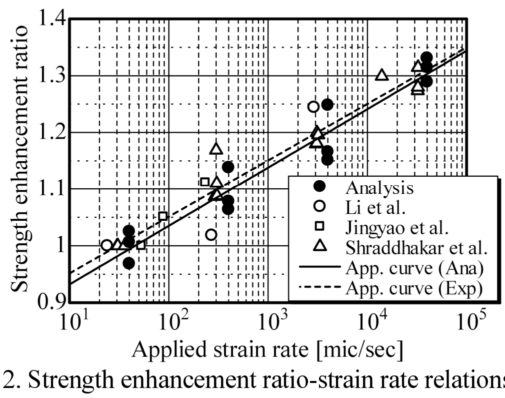

Figure 12. Strength enhancement ratio-strain rate relationships.

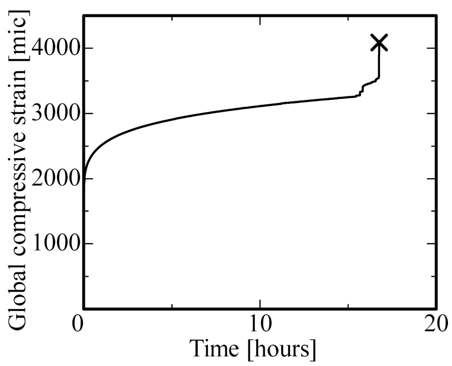

Figure 13. Global strain-time relationship under creep loading in compression (CC80).

4.3.1 *Global strain-time relationships*

Figure 13 and 14 show global strain-time relationship obtained in CC80 and CT, respectively. The analyses finished when the pseudo monotonic loading analysis shown in Figure 9 made failure determination at the X marked point. Shape of the curve became convex upward first, lineally increased second, and accelerated around the failure point. That is, progression of creep strain up to the failure can be divided into 3 stages, which are transient, steady and accelerating state, as observed in the experiment.

Figure 15 shows global strain-time relationship obtained in CC14.8MPa and CC10.2MPa. Experimental result by Neville (1959) is also shown in the figure. In both cases, creep recovery behavior could be simulated. This strain recovery was derived from delayed reversible deformation of visco-elastic component.

4.3.2 *Investigation on fracture mechanism*

Figure 16 shows failure state in case TC. Horizontal crack as shown in the figure led to the failure. To investigate mechanical behavior in meso level, connected springs across the cutting surface I-I', II-II' and III-III' were picked up, and vertical resisting forces *S* of the sections were calculated using stresses of the springs (See Fig. 16). Figure 17 shows change of the vertical resisting force in each section. Where, the point of t=44sec, 140days, 464days, 480days are corresponding to the circular dots and X marked point in the Figure 14. That is, t=0 to 44sec, t=44sec to 140days, t=140days to 464days and t=464days to 480days are corresponding to initial loading, transient creep, steady state creep and accelerating creep, respectively. Though there are no cracks above the horizontal crack, vertical resisting forces decreased over time in the section II-II' and III-III'. This is because of relaxation derived from visco-elastic and visco-plastic component.

This study determines a fracture process of mortar under creep loading as shown in Fig. 18. As shown in (a), the horizontal crack is modeled in wedge shape and a free-body ABCDD' is considered. Where, point D represents the crack tip and distance from point D to D' is minutely small. Next, forces applied to the free-body ABCDD' is considered (b). When creep loading starts (t=44sec), tensile stress σ_t, tension softening stress due to crack opening σ_{ts}, stress at the crack tip σ_{tip} and vertical resisting force *S* are applied to the section A-B, C-D, D-D' and A-D', respectively. Vertical resisting force *S* decreases over time because of the relaxation as mentioned before (*S* becomes S-ΔS). Stress ΔS released from the section A-D' is totally redistributed to the crack tip D-D' to satisfy force equilibrium against the applied external force because stress in the section C-D cannot increase in softening state. As a result, stress at the crack tip increases as shown in (c) (σ_{tip} becomes σ_{tip}+$\Delta\sigma_{tip}$). At that time, if stress at the crack tip reaches to tensile strength, the horizontal crack propagates to depth direction. Repeating the above process, the crack develops over time and global failure happens when the material strength becomes less than the applied stress.

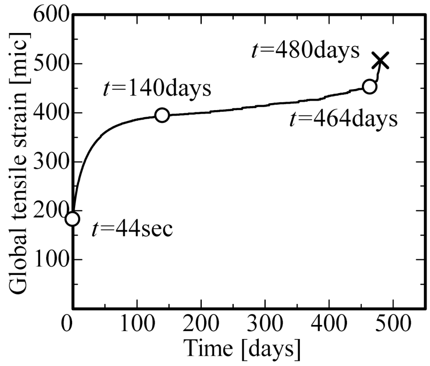

Figure 14. Global strain-time relationship under creep loading in tension (CT).

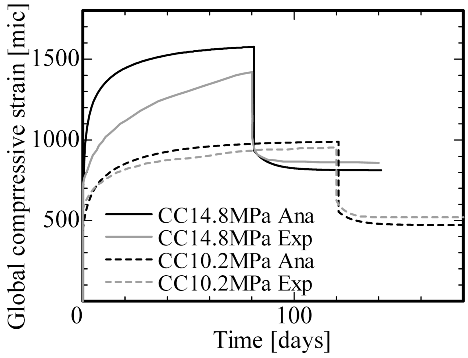

Figure 15. Global strain-time relationship under creep loading with unloading (CC14.8MPa and CC10.2MPa).

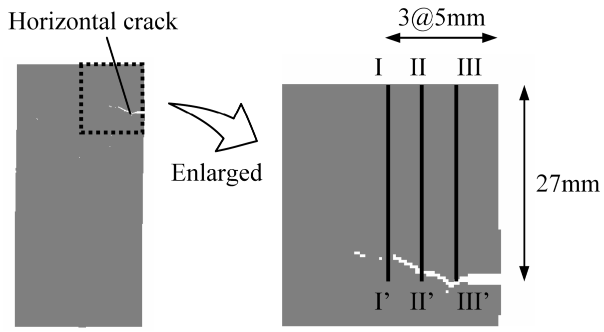

Figure 16. Failure state and location of the cutting face in TC (*Deformation x 50*).

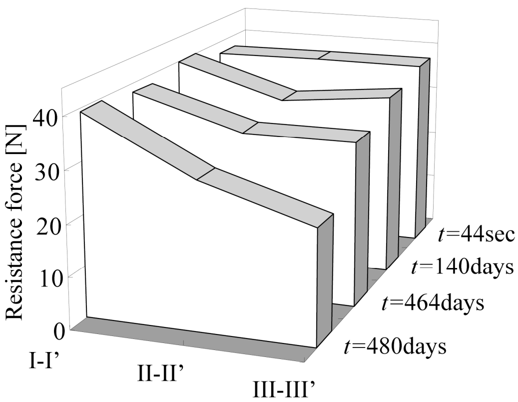

Figure 17. Change of vertical resisting force in the cutting faces in TC.

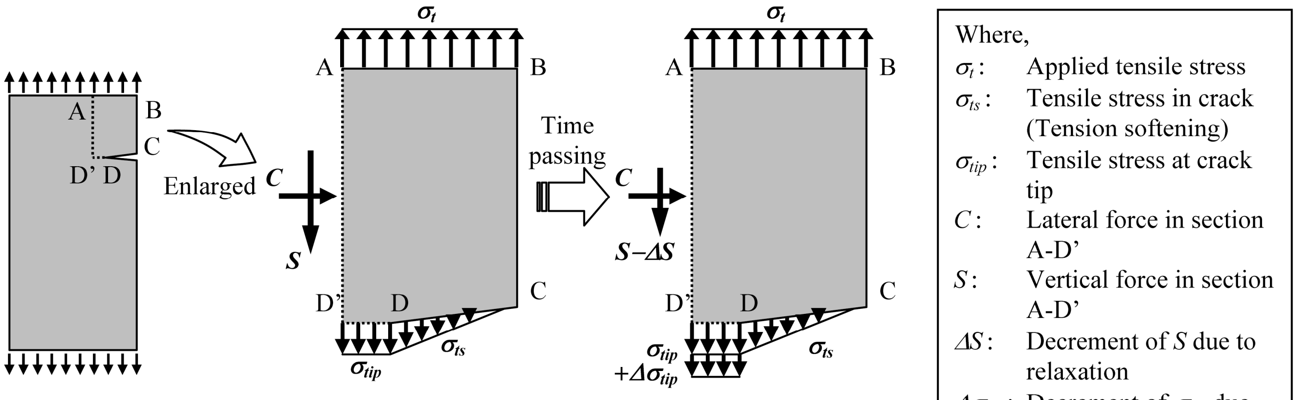

(a) Schematic illustration of horizontal crack | (b) Forces on ABCDD' (When creep loading starts) | (c) Forces on ABCDD' (After time passed)

Figure 18. Modeling of horizontal crack and transition of force distribution under creep loading.

5 CONCLUSIONS

The following conclusions were obtained in this study.

1) Time-dependent constitutive law, in which mortar deformation is divided into elastic, visco-elastic, visco-plastic and cracking component based on material structure from micro to meso level, was developed and introduced into RBSM. The analytical model proposed in this study can express deformation and fracture process of mortar under time-dependent loads.

2) The analytical model could simulate strength enhancement of mortar in compression under higher strain rates. Besides, it could express variation of the results as well with introducing variation of material properties in meso level using the probability density function. Degree of the variation in the analyses was smaller than that in the experiment. This is because the experimental results contain factors other than strength variation (e.g. loading accuracy and environmental condition).

3) The analytical model could simulate basic characteristics of mortar under high stress creep loading. Using a new method for determining failure for load-controlled analysis, fracture process that is composed of transient creep, steady state creep and accelerating creep could be expressed. In addition, for low stress creep loading, not only creep strain-time curve but also creep recovery behavior could be well simulated comparing with the experimental result.

4) Mortar failure under creep loading is caused by not only cracking component but also visco-elastic and visco-plastic component that are reversible and irreversible time-dependent deformation. Based on the investigation of change in sectional resisting force around the crack, a fracture mechanism, which stress redistribution caused by relaxation due to visco-elastic and visco-plastic component leads new cracks to be formed, was determined.

ACKNOWLEDGEMENT

This study was supported by 21st Century COE Program "Sustainable Metabolic System of Water and Waste for Area-based Society" and the Grant-in-Aid for Scientific Research (A) No. 19206048, both of which are granted by Japanese Government. The authors also would like to show their gratitude to the Center for Concrete Corea, Korea through the Yonsei University for its financial support.

REFERENCES

Cundall, P.A. & Strack, O.D.L. 1979. A discrete numerical model for granular subassemblies. *Geothechnique* 29:47-65.

Bolander, J.E. & Saito, S. 1998. Fracture analysis using spring network models with random geometry. *Engineering Fracture Mechanics* 61: 569-591.

El-Kashif, K.F. & Maekawa, K. 2004. Time-dependent nonlinearity of compression softening in concrete. *Journal of Advanced Concrete Technology* 2(2): 233-247.

Hatano, T. 1962. Behavior of concrete by cyclic compression load. *Proceedings of JSCE* 84: 19-28. (in Japanese)

Jingyao, C. & Chung, D.D.L. 2002. Effect of strain rate on cement mortar under compression, studied by electrical resistivity measurement, *Cement and Concrete Research* 32: 817-819.

Kawai, T. 1977. New element models in discrete structural analysis. *Journal of Society of Naval Architectures Japan* 141: 187-193.

Li, Z. & Huang, Y. 1998. Effect of strain rate on the compressive strength surface cracking and failure mode of mortar. *ACI Material journal* 95(5): 512-518.

Maekawa, K., Toongoenthong, K., Gebreyouhannes, E. & Kishi, T. 2006. Direct path-integral scheme for fatigue simulation of reinforced concrete in shear. *Journal of Advanced Concrete Technology* 4(1): 159-177.

Matsumoto, K., Sato, Y., Ueda, T. & Wang, L. 2008. Mesoscopic analysis of mortar under high-stress creep and low-cycle fatigue loading. *Journal of Advanced Concrete Technology* 6(2): 337-352.

Muguruma, H. & Tominaga, M. 1970. Stress-strain relations of concrete under repeated over-load. *Journal of the Society of Materils Science, Japan* 19(200): 1-10. (in Japanese)

Nagai, K., Sato, Y & Ueda, T. 2004. Mesoscopic simulation of failure of mortar and concrete by 2D RBSM. *Journal of Advanced Concrete Technology* 2(3): 359-374.

Neville, A. M. 1959. Creep recovery of mortars made with different cements. *Jounral of the American Concrete Institute* 31(2): 167-174.

Shraddhakar, H., Zhenjia, S. & David, D. 1990. Strain-rate sensitive behavior of cement paste and mortar in compression. *ACI Material journal* 87(5): 508-516.

Sugihara, K. 1998. Fortran computational geometry programming. Tokyo: Iwanami shoten. (in Japanese)

Tanabe, T., Ishikawa, Y. & Ando, N. 1998. Visco-elastic and visco-plastic modeling of transient concrete. *Computational modeling of concrete structures* 1: 441-453.

Ueda, M., Kei, T. & Taniguchi, H. 1988. Discrete limit analysis of reinforced concrete structures by RBSM. *Proceedings of Japan Concrete Institute* 10(3): 335-338. (in Japanese)